Non-linear response of colloid monolayers at high-frequency probed by ultrasound-driven microbubble dynamics

Saha, Saikat; Luckham, Paul F.; Garbin, Valeria

DOI
10.1016/j.jcis.2022.10.093

Publication date
2023

Document Version
Final published version

Published in
Journal of Colloid and Interface Science

Journal of Colloid and Interface Science 630 (2023) 984–993

Contents lists available at ScienceDirect

Journal of Colloid and Interface Science

journal homepage: www.elsevier.com/locate/jcis

Non-linear response of colloid monolayers at high-frequency probed by ultrasound-driven microbubble dynamics

Saikat Saha [a,b], Paul F. Luckham [b], Valeria Garbin [a,b,*]

[a] Department of Chemical Engineering, Delft University of Technology, 2629 HZ Delft, the Netherlands
[b] Department of Chemical Engineering, Imperial College London, London SW7 2AZ, United Kingdom

GRAPHICAL ABSTRACT

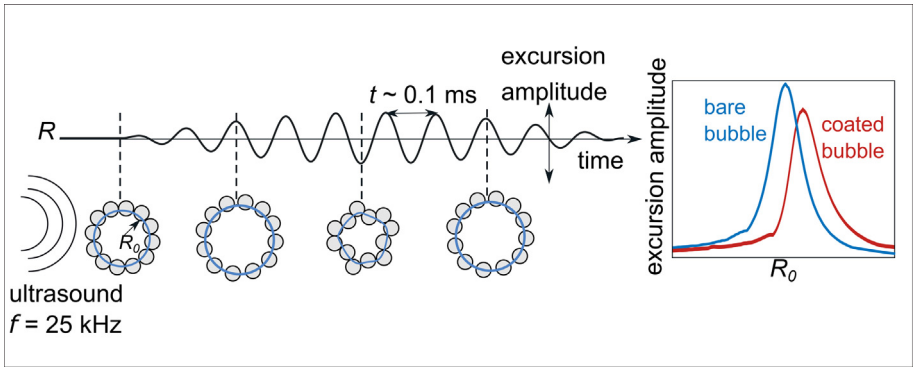

ARTICLE INFO

Article history:
Received 18 June 2022
Revised 30 September 2022
Accepted 17 October 2022
Available online 22 October 2022

Keywords:
Interfacial rheology
Colloids
Bubbles
Ultrasound

Hypothesis: High-frequency interfacial rheology of complex interfaces remains challenging yet it is central to the performance of multiphase soft matter products. We propose to use ultrasound-driven bubble dynamics to probe the high-frequency rheology of a colloid monolayer used as model system with controlled interactions and simultaneous monitoring of the microstructure. We hypothesize that by comparing the response of colloid-coated bubbles with that of a bare bubble under identical experimental conditions, it is possible to detect the non-linear response of the monolayer and use it to extract interfacial rheological properties at $10^4 s^{-1}$.

Experiments: Using high-speed video-microscopy, the dynamics of colloid-coated bubbles were probed to study the micromechanical response of the monolayer to high-frequency deformation. Protocols analogous to stress-sweep and frequency-sweep were developed to examine the stress–strain relationships. A simple model, motivated by the observed non-linear responses, was developed to estimate the interfacial viscoelastic parameters.

Findings: The estimated elastic moduli of colloid monolayers at $10^4 s^{-1}$ are about an order of magnitude larger than those measured at 1 s^{-1}. The monolayers exhibit non-linear viscoelasticity for strain amplitudes as small as 1%, and strain-softening behaviour. These findings highlight the applicability of acoustic bubbles as high-frequency interfacial probes.

* Corresponding author at: Department of Chemical Engineering, Delft University of Technology, 2629 HZ Delft, the Netherlands.
E-mail address: v.garbin@tudelft.nl (V. Garbin).

https://doi.org/10.1016/j.jcis.2022.10.093
0021-9797/

1. Introduction

The rheological properties of complex fluid interfaces strongly affect the macroscopic behaviour of multiphase systems [1,2], and are central in many industrial processes and products [3–6]. Two main approaches have been used to develop methods for interfacial rheology: the first has been to adapt bulk rheological techniques to interfaces [7], the second has been to extend methods of interface science to measure interfacial rheology [8,9]. A limitation of the first approach is that the only mode of deformation that can be applied is shear, but interfaces are highly compressible and therefore dilational rheology is central to their behaviour [1]. The methods of interface science on the other hand produce dilational deformation, but are limited in the deformation rates for which the Young–Laplace equation, valid for static equilibrium, can be used to analyze the data. Pendant drop elastometry [10–12] and Langmuir trough methods [13,14] have typical deformation rates of $10^{-2} - 1s^{-1}$ which have limited applicability in dynamic settings, and cannot access the high strain rates of industrial processing flows [15]. Moreover, the effect of the flow induced in the adjacent liquid phases upon deformation of the interface needs to be correctly accounted for [7], and artefacts in the measurement can occur if the dilation is non-uniform and Marangoni stresses arise due to concentration gradients at the interface. Lastly, relating the mechanical response of a complex interface to the microstructure has only been possible in relatively slow dynamic settings [9,16,3,4], in order to accurately resolve the microstructure in space and time. Yet, the deformation rate can cause dramatic differences in the fate of interfacial layers [17]. A few methods have been demonstrated for the characterisation of interfaces at high frequency of deformation, for instance surface wave propagation measured by light scattering [18], analysis of droplet shape oscillations [19], or analysis of the oscillations of photothermally activated plasmonic microbubbles [20].

Bubble dynamics in soft matter [21] are emerging as a platform for high-frequency and high-strain rate rheology [22–25]. Ultrasound-driven microbubble dynamics have been used to measure the high-frequency viscoelastic properties of lipid monolayers on the bubble interface for biomedical ultrasound applications [26,20], but the potential for broader applicability in interfacial rheology remains largely unexplored. An ultrasound-driven bubble offers the advantages of applying isotropic area deformation at a selected driving frequency in the range of kHz-MHz, which is inaccessible with most methods. Furthermore the kinematics of spherical bubble deformation are such that bulk stresses are always normal to the interface; and optical or confocal microscopy can be used for monitoring the microstructure [24].

Here we apply ultrasound-driven bubble dynamics for high-frequency interfacial rheology of colloid monolayers. Colloid-coated bubbles have often been used as a model system to understand the dynamics of complex interfaces [27–31], because the interparticle interactions can be controlled and the microstructure directly visualized. We propose and test two different protocols: an acoustic pressure sweep, akin to a stress sweep; and a radius sweep, which is equivalent to a frequency sweep. Using high-speed video-microscopy, we record the time-dependent bubble size and shape. The oscillatory dynamics of both coated and bare bubbles are compared under identical conditions to decouple the non-linear effects due to the interfacial layer. A simple constitutive model is proposed which captures the observed non-linear response of the monolayer. The model enables one to extract elastic moduli at high frequency. The values are compared to low-frequency measurements performed using drop-shape analysis. The protocols developed here are generally applicable to study the response and test constitutive models for high-frequency deformation with a range of surface-active agents including polymers and proteins.

2. Model for colloid-coated bubble dynamics in ultrasound

2.1. Background on bubble dynamics in ultrasound

Bubbles respond to the periodic changes in pressure caused by an acoustic wave by undergoing periodic compression and expansion. The time-dependent radius of the bubble, $R(t)$, is governed by the Rayleigh-Plesset equation [32], modified here to account for surface tension and compressibility effects:

$$\rho\left(R\ddot{R}+\frac{3}{2}\dot{R}^2\right)=\left(p_0+\frac{2\sigma}{R_0}\right)\left(\frac{R_0}{R}\right)^{3\kappa}\left(1-\frac{3\kappa\dot{R}}{c}\right)-p_0-p_{ac}(t)-\frac{2\sigma}{R}-4\mu\frac{\dot{R}}{R} \quad (1)$$

In Eq. (1), the dots denote derivatives with respect to time, ρ is the density of the liquid, p_0 is the ambient pressure, $p_{ac}(t)=\Delta p\sin(\omega t)$ is the acoustic pressure, with amplitude Δp and angular frequency $\omega=2\pi f$, σ is the surface tension of the gas–liquid interface, R_0 the equilibrium radius of the bubble, κ the polytropic exponent, and μ the viscosity of the liquid. The terms on the left-hand side account for the inertia of the liquid. The first term on the right-hand side of Eq. (1) describes the compression of the gas inside the bubble through a polytropic relationship [33] and the effect of liquid compressibility when the ratio $\dot{R}/c$, with c the speed of sound in the liquid, is not negligible. The fourth term on the right-hand side accounts for the Laplace pressure and the last term for viscous dissipation in the fluid.

For small forcing amplitude, $\Delta p \ll p_0$, the bubble behaves as a linear harmonic oscillator [32], with a natural frequency, ω_0, given by:

$$\omega_0^2=\frac{1}{\rho R_0^2}\left[3\kappa p_0+\frac{2(3\kappa-1)\sigma}{R_0}\right]. \quad (2)$$

The resonant behaviour of the bubble is described by its resonance curve, that is, the amplitude of oscillations x_0 as a function of frequency ω:

$$x_0(\omega)=\frac{\Delta p}{\rho R_0^2}\frac{1}{\sqrt{\left(\omega^2-\omega_0^2\right)^2-4\beta^2\omega^2}}, \quad (3)$$

where β is the total damping coefficient including viscous, thermal, and acoustic radiation effects [33].

2.2. Background on models for coated-bubble dynamics

Modifications of the Rayleigh-Plesset equation have been proposed to account for the effect of a coating on bubble dynamics, especially in the context of lipid-coated microbubbles for biomedical ultrasound. Depending on the nature of the interfacial layer, the coated interface may exhibit interfacial viscosity, interfacial elasticity, or both. Early models were proposed for a continuous viscoelastic solid of finite thickness [34]. A model accounting for the elasticity and viscosity of a lipid monolayer, but also for the characteristic non-linear response during compression, namely monolayer buckling, was developed by Marmottant et al. [35] and is often referred to as the "Marmottant model". In this model, the effective surface stress $\sigma(R)$ and the surface dilational viscosity η_d are incorporated into the modified Rayleigh-Plesset equation to give [35]:

$$\rho\left(R\ddot{R}+\frac{3}{2}\dot{R}^2\right)=\left[p_0+\frac{2\sigma(R_0)}{R_0}\right]\left(\frac{R_0}{R}\right)^{3\kappa}\left(1-\frac{3\kappa\dot{R}}{c}\right)-p_0 - p_{ac}(t)-\frac{2\sigma(R)}{R}-\frac{4\eta_d\dot{R}}{R^2}-\frac{4\mu\dot{R}}{R}. \quad (4)$$

In Eq. 4, $\sigma(R)$ is the constitutive equation for the dependence of the surface elastic stress on the radius of the bubble, and interfacial viscous effects are described by the dilational viscosity η_d. For coated bubbles, η_d contributes to the total damping coefficient in Eq. (3) [26]. To account for the observed non-linear behavior of phospholipid monolayers, which buckle out of plane during compression [36], the following piece-wise constitutive equation for the effective surface elastic stress was proposed in [35]:

$$\sigma(R)=\begin{cases}0 & \text{if} \quad R\leqslant R_{buckling},\\ \sigma(R_0)+E_d\left(\frac{R^2}{R_{buckling}^2}-1\right) & \text{if} \quad R_{buckling}<R<R_{break},\\ \sigma_{water} & \text{if} \quad R\geqslant R_{break}.\end{cases} \quad (5)$$

Eq. (5) includes a linear regime of deformation with constant elastic modulus E_d; outside of this linear regime, non-linear phenomena are described phenomenologically by setting the surface stress to approach the value of the bare gas–water interface, σ_{water}, when the monolayer breaks upon large expansion (for radii $R\geqslant R_{break}$), and to approach zero when the interfacial layer buckles upon strong compression (for radii $R\leqslant R_{buckling}$). The surface elasticity, E_d, affects the natural frequency, resulting in [26]:

$$\omega_0^2=\frac{1}{\rho R_0^2}\left[3\kappa p_0+\frac{2(3\kappa-1)\sigma(R_0)}{R_0}+\frac{4E_d}{R_0}\right]. \quad (6)$$

The change in resonance frequency due to surface elasticity is measurable when $2\sigma(R)/R\sim 4E_d/R$, which corresponds to $E_d\sim 0.5$N/m for $R_0\sim 100\mu$m. This model, which effectively describes the lipid monolayer as tensionless during compression, captures the *compression-only* behaviour of lipid-coated bubbles observed in experiments [37,38], where the extent of bubble compression is larger than its expansion.

2.3. Constitutive model for colloid-coated interface

For colloid-coated bubbles, *expansion-only* behaviour has been reported in experiments on microbubbles with liposomes attached to their surface [39], and bubbles coated with micron-sized colloids [28]. Microscopic observations during quasi-static compression of a colloid-coated bubble revealed that the layer resists compression by undergoing different buckling modes [29]. During monolayer compression beyond full coverage, some particles are pushed out of plane by a distance of the order of the particle radius a, leading to a staggered pattern. This configuration is energetically unfavorable, due to the large capillary energy ($\sim 10^6 k_BT$) that tends to restore the equilibrium position of the particles at the interface [40] resulting in high resistance to in-plane compressive stresses. A particle monolayer is thus able to withstand collapse until a higher critical pressure than is estimated using a continuum approach [27,29]. This deformation regime may be referred to as *local* [29] or *particle-scale* buckling (length scale $\sim a$). Upon further compression, the monolayer undergoes *large-scale* buckling that can be visible with the naked eye [41] or comparable to the bubble/droplet size, with length scale $\sim R_0$ [27,29,42] and analogous to the buckling regime reported for lipid monolayers [36].

We propose to modify the constitutive model developed by Marmottant et. al. [35] for the surface elastic stress, Eq. (5), to account for the resistance of a colloid monolayer against compression. We propose a regime that describes the fact that when the monolayer is compressed beyond full coverage (radii $R<R_{full}$), the surface stress can be described in terms of an effective compression modulus K_d based on the projected area of the monolayer. The overall surface stress within the colloid monolayer can then be expressed as:

$$\sigma(R)=\begin{cases}\sigma(R_{full})+K_d\left(\frac{R^2}{R_{full}^2}-1\right), & \text{if} \quad R\leqslant R_{full}\\ \sigma(R_{full})+E_d\left(\frac{R^2}{R_{full}^2}-1\right), & \text{if} \quad R_{full}<R<R_{break}\\ \sigma_{water}, & \text{if} \quad R\geqslant R_{break},\end{cases} \quad (7)$$

as schematically represented in Fig. 1. At full surface coverage, the effective surface tension for a colloid monolayer $\sigma(R_{full})$ is non-zero [43,28]. For coated bubbles with high surface coverage, it is reasonable to assume $R_0\approx R_{full}$ and the regimes are simplified as in Eq. 7 (details in Supplementary Material). In the rest of the paper we refer to this approach, Eq. 7, as the "extended Marmottant model". In this model, for compression beyond full coverage, the surface stress continues to decrease until it becomes negative, consistent with the fact that internal stresses in the monolayer tend to expand it to attain a more relaxed configuration [44,27,45]. This compression regime continues until the monolayer undergoes large-scale buckling, for which colloid monolayers are usually reported to undergo compression at constant surface pressure [41,42,46]. The regime of large-scale buckling (see Eq. 5) is not included in the constitutive model because it is outside of the range of our experiments.

3. Materials and methods

3.1. Preparation of colloid-coated bubbles

Sulfate-functionalised, polystyrene latex microspheres with nominal diameters $2a=2.4\mu$m, 5μm and 10μm were obtained from Molecular Probes (Invitrogen, Thermo Fisher Scientific). The stock suspension was diluted with a 500 mM solution of NaCl (VWR Chemicals) in ultrapure water (resistivity 18.2MΩ cm; Merck Millipore-Milli-Q Integral 3 system), thereby screening the electrostatic repulsion between the particles and promoting adsorption to the water–gas interface. The particles form a cohe-

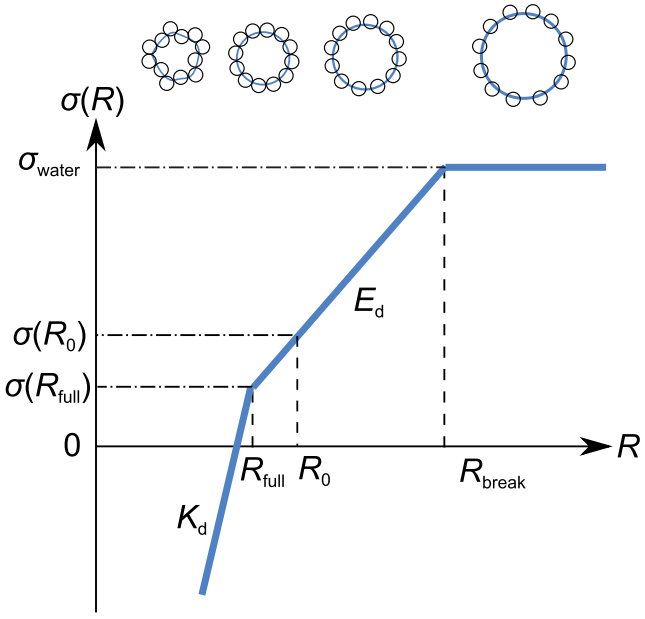

Fig. 1. Schematic of the proposed constitutive model for the surface elastic stress for a colloid-coated bubble as a function of bubble radius, $\sigma(R)$.

sive monolayer at the gas liquid–gas interface, due to attractive interparticle interactions, namely van der Waals interactions, and capillary interactions due to nm-scale undulations of the contact line, as described in previous work on the same system [31]. Dispersions with concentrations of 0.4 w/v% for the 2.4 and 5μm particles and 0.8 w/v% for the 10μm particles were used to make particle-stabilised bubbles by agitation using a vortex mixer (PV-1, Grant) at 3000 rpm for 2 min. This protocol produces polydisperse, particle-coated bubbles with full coverage of particles at the interface, as previously reported for armoured bubbles [27,29,45]. The particle-coated bubbles remained stable for several weeks at room temperature, or months when refrigerated at 2–8°C.

3.2. Geometry for bubble oscillation experiments

In experiments on bubble dynamics, the proximity of a liquid–gas or liquid–solid boundary is difficult to avoid because the buoyancy force causes bubbles to rise to the top of the sample. Boundaries made of soft hydrogels have been shown to cause minimal influence on bubble dynamics [47,48] due to their very small acoustic impedance mismatch with water. We therefore designed a geometry [see Fig. 2(a)] in which the bubble rests against a hydrogel-water boundary, and all rigid boundaries are sufficiently far from the bubble (at least 20 bubble diameters away) so as to not affect the dynamics. The hydrogel geometry was made using 2% w/v agarose (Sigma–Aldrich) and the cavity where the bubble was placed was moulded as a spherical cap in order to align the bubble in the centre of the geometry.

For each experiment, a single bubble was injected into the geometry, filled with 500 mM NaCl (aq) solution, where it rested against the concave ceiling. The geometry was then sealed using a glass cover slip. Microscopy imaging confirmed that the bubble was fully coated with particles, as shown in Fig. 2(b). To introduce a bare bubble, a small air pocket was released into the liquid-filled geometry using a syringe, and then sealed with the cover slip. To control the bubble size, we took advantage of bubble dissolution due to gas diffusion, and waited until the bubble had dissolved to the desired radius R_0.

3.3. Experimental setup

A schematic of the experimental setup is presented in Fig. 2(a). A piezoelectric actuator (P141.10, Physik Instrumente Ltd.) glued onto a glass plate was used to transmit ultrasound waves to the sample. Polydimethylsiloxane (PDMS, 10:1 elastomer to curing agent, Dowsil Sylgard 184, Univar Ltd.) spacers were used to support the glass plate, under which the hydrogel geometry was mounted. The unit was mounted on an inverted microscope (IX71, Olympus). An arbitrary waveform generator (33220A, Agilent Technologies, Inc.), linked to a power amplifier (AG 1021 Linear Amplifier, T&C Power Conversion, Rochester, USA) and a triggering unit (Sapphire 9214, Quantum composers, Inc.), was programmed to send a 10-cycle sine-enveloped sine wave. The

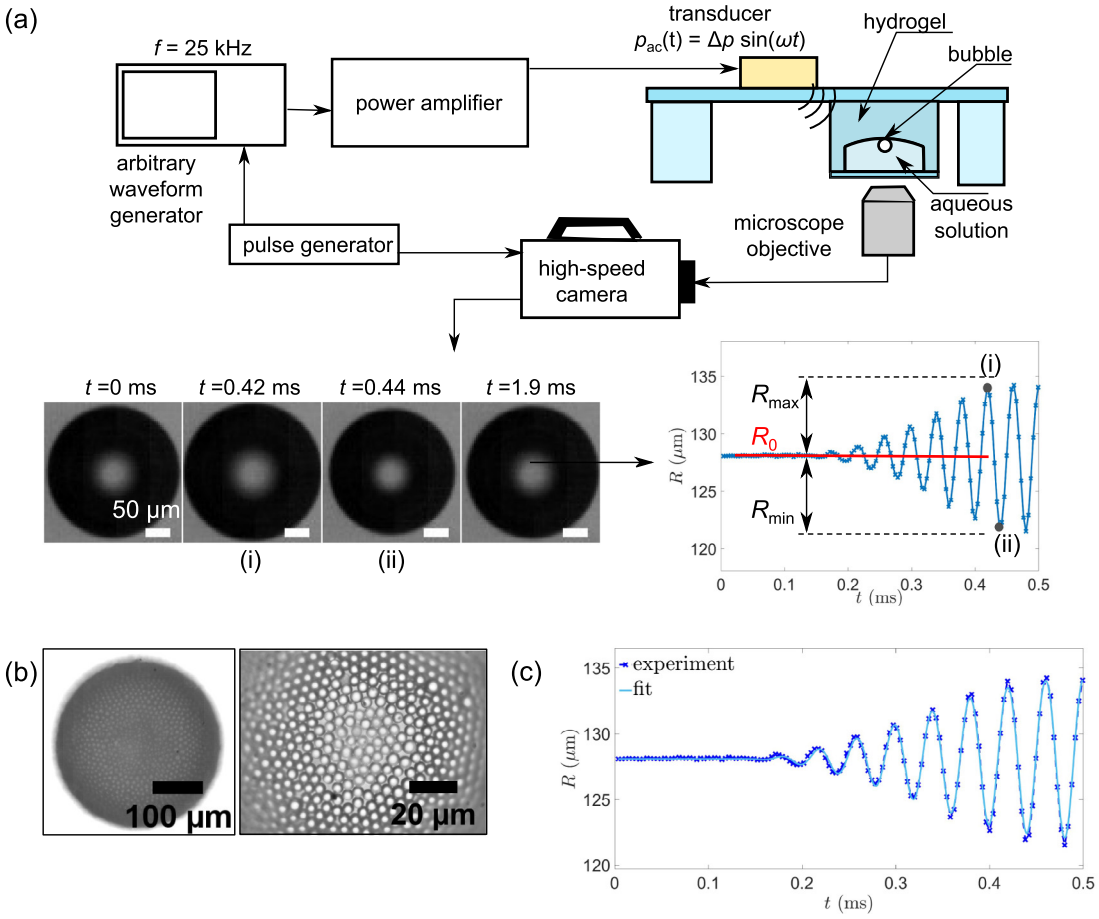

Fig. 2. Experimental setup and methods. (a) A schematic of the acousto-optical setup for acoustic forcing and time-resolved imaging of bubbles. An example of a recording of a bare bubble is shown along with the resulting radius-time curve following image analysis. The error bars on R are smaller than the symbols. (b) Optical micrographs of colloid-coated bubbles at different magnifications to highlight the microstructure at the interface. Colloids are 5μm in diameter. (c) Fitting the Rayleigh-Plesset equation to a bare bubble radius-time curve obtained from an experiment. Only the driven part of the oscillations are fitted. The fitting parameters are $\Delta p = 1.24$ kPa, $\kappa_{eff} = 1.3$ and $\mu_{eff} = 2.8$mPa.s.

driving frequency for the signal was $f = 25$kHz. The pulse-delay generator triggered a high-speed camera (FASTCAM SA5, Photron, Ltd.), recording at 262,500 frames per second, and the waveform generator, with a 100μs delay between them, to allow the observation of the onset of transient bubble oscillations.

3.4. Image analysis

The bubble radius was tracked in each frame of the videos. An optimal threshold for binarisation was determined for each frame using the *greythresh* function in MATLAB (The MathWorks Inc., Natick, Massachusetts, United States). Particles around the bubble were removed from the processed image using morphological operations with the *bwmorph* function. For the case of bare bubbles, which have a central bright region, the *imfill* function was used to fill this region in the binarised images. From the binarised images, the 2D projected area of a bubble in the focal plane was obtained by counting the number of pixels within the bubble. From this projected area, an equivalent radius was calculated. With this image analysis routine, the radius is tracked with sub-pixel resolution. Varying the threshold for binarisation by 5% around the optimal value results in a variation in the determined radius of typically $\pm 0.4\mu$m. This is taken as the uncertainty on the measured radius.

3.5. Measurement of acoustic pressure amplitude

Bare bubbles were used as probes to calibrate the acoustic pressure amplitude at the location of the bubble in the liquid-filled cavity, Δp, by fitting Eq. (1) to a time series of radial oscillations, $R(t)$, as shown in Fig. 2(c). The pressure could not be measured directly using a hydrophone due to the small size of the geometry. The effect of the hydrogel surface in contact with the bubble is known to be minimal [48]. Small elastic and viscous contributions from the hydrogel boundary were effectively lumped in the fitting parameters: the acoustic pressure amplitude Δp, the polytropic exponent κ_{eff}, the viscosity μ_{eff}, and the start-time t_s, defined as the time when the bubble starts oscillating. The Rayleigh-Plesset equation was fitted to the experimental radius-time curves using non-linear global optimisation routines in MATLAB. Only the driven part of the oscillations was considered for curve fitting. The values of start time, t_s, for bubbles of the same size were found to be within 1% of each other thanks to the convex geometry designed to position all bubbles at the same location. For each new geometry, Δp was calibrated against the amplifier gain $A(\%)$ by curve-fitting to at least 20 time series of bare bubble oscillations. Henceforth, all results are presented in terms of calibrated pressure amplitude Δp. The calibration for the geometry used for Figs. 3, 4, and Fig. 5 is $\frac{\Delta p}{A} = (15.6 \pm 2.2)\frac{\text{Pa}}{\%}$. The calibration for the geometry used in Fig. 6 is $\frac{\Delta p}{A} = (9.4 \pm 0.8)\frac{\text{Pa}}{\%}$. The estimated κ_{eff} and μ_{eff} are found to be dependent on R_0, but independent of Δp. These parameter estimates are then used for the coated bubbles when comparing with the models.

3.6. Radius-sweep protocol

To obtain an experimental resonance curve, a *frequency sweep* is typically performed [26,22] in which the maximum excursion, x_0, is measured as a function of frequency, ω, to obtain $x_0(\omega)$. The maximum excursion is defined as

$$x_0 = \frac{R_{\max} - R_{\min}}{2R_0}, \tag{8}$$

with $R_{\max}$ and $R_{\min}$ the maximum and minimum bubble radii attained during the oscillations, respectively. Because varying the frequency would modify the pressure field in the geometry, we performed experiments at a fixed driving frequency. In this case a resonance curve can be obtained by performing a *radius sweep*, that is, by varying the bubble radius R_0 and measuring the maximum excursion from each oscillation run to generate a resonance curve $x_0(R_0)$ [49,48,23]. Typically, a bare bubble with initial equilibrium radius $R_0 \approx 250\mu$m was introduced into the enclosure and allowed to dissolve. The bubble was driven into oscillations with the 10-cycle pulse, then allowed to dissolve for 1 min, then driven again. The duration of the 10-cycle pulse, 0.4 ms, is much shorter than the timescale over which the radius changes due to dissolution. This way, as R_0 decreased from 250μm to 50μm, the oscillations were recorded for $n \approx 40$ values of the equilibrium radius R_0. For colloid-coated bubbles, which were too stable to dissolve, the radius was varied by introducing in the geometry a different bubble with different equilibrium radius R_0 each time. Each bubble was subjected to three 10-cycle pulses, with an interval of 1 min in between, to measure the average and standard deviation in the excursion amplitudes.

3.7. Pressure-sweep protocol

We also performed *pressure sweep* experiments, in which the acoustic pressure amplitude Δp was varied for a constant bubble size R_0 at constant frequency. In the linear regime [33], which for bare bubbles is for $\Delta p \ll p_0$, the excursion amplitude is proportional to the forcing amplitude. This protocol can therefore be used to evidence non-linear phenomena due to the interfacial monolayer. The same bubble was forced with the 10-cycle pulse for a set of different pressure amplitudes Δp. The number of runs was selected so that, over the course of all the runs, the equilibrium radius remained constant to within $\approx 1 - 2\%$. Hence for smaller bubbles, which dissolve faster, fewer runs were performed. The acoustic amplitudes used were always sufficiently small to prevent particle expulsion from the monolayer, which is observed for large-amplitude oscillations [28]. Finally, using a small number of acoustic cycles ensures that hydrodynamic interactions between the particles [31] are negligible.

4. Experimental results and discussion

4.1. Calibration experiments with bare bubbles

Fig. 3 presents the results of calibration experiments on bare bubbles for both protocols introduced in Section 3. Fig. 3(a) shows the results of a radius sweep of 9 different bare bubbles, each driven with a different acoustic pressure amplitude, in the range $\Delta p = 0.16 - 1.41$ kPa. Fig. 3(b) shows the result of a pressure sweep for a bare bubble. Within the range of pressures used, the excursion amplitude increases linearly with pressure, a signature of linear behaviour. The data points nearly overlap for both sweeps with increasing (open symbols) and decreasing (solid symbols) pressure.

Furthermore, taking a vertical line in the resonance map of Fig. 3(a) for a given R_0, provides the excursion amplitudes as a function of pressure for that bubble size. Overlaying these data points for $R_0 = 133.8\mu$m onto the pressure sweep of Fig. 3(b), confirms that radius sweep and pressure sweep give consistent results. Additional datasets showing repeatability of these results are provided in the Supplementary Material (Figures S1–S3).

4.2. Expansion-only behaviour of colloid-coated bubbles

Fig. 4(a) shows that colloid-coated bubbles buckle during compression. As seen in Fig. 4(b,c), colloid-coated bubbles exhibit

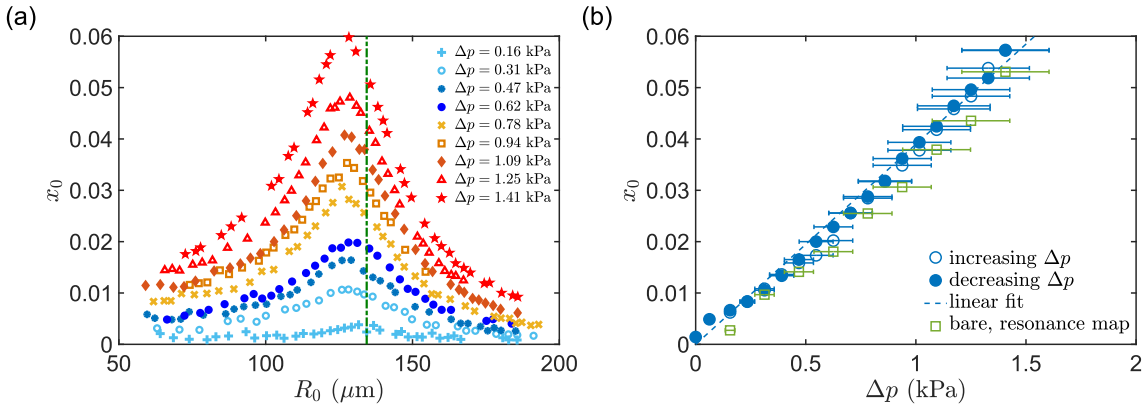

Fig. 3. Radius sweep and pressure sweep for bare bubbles. (a) Radius-sweep for bare bubbles at different pressures, resulting in a map of excursions x_0 for different radii R_0 at different Δp. (b) Pressure-sweep on a bare bubble of radius $R_0 = 133.8\mu$m for pressure going up (open circles); pressure going down (filled circles) with the linear fit to the data (blue dashed line). The $x_0 - \Delta p$ data for the same bubble radius (open squares), obtained from linear interpolation of the data in the resonance map [see vertical green-dashed line in (a)] is also shown. The error bars on x_0 are smaller than the symbols.

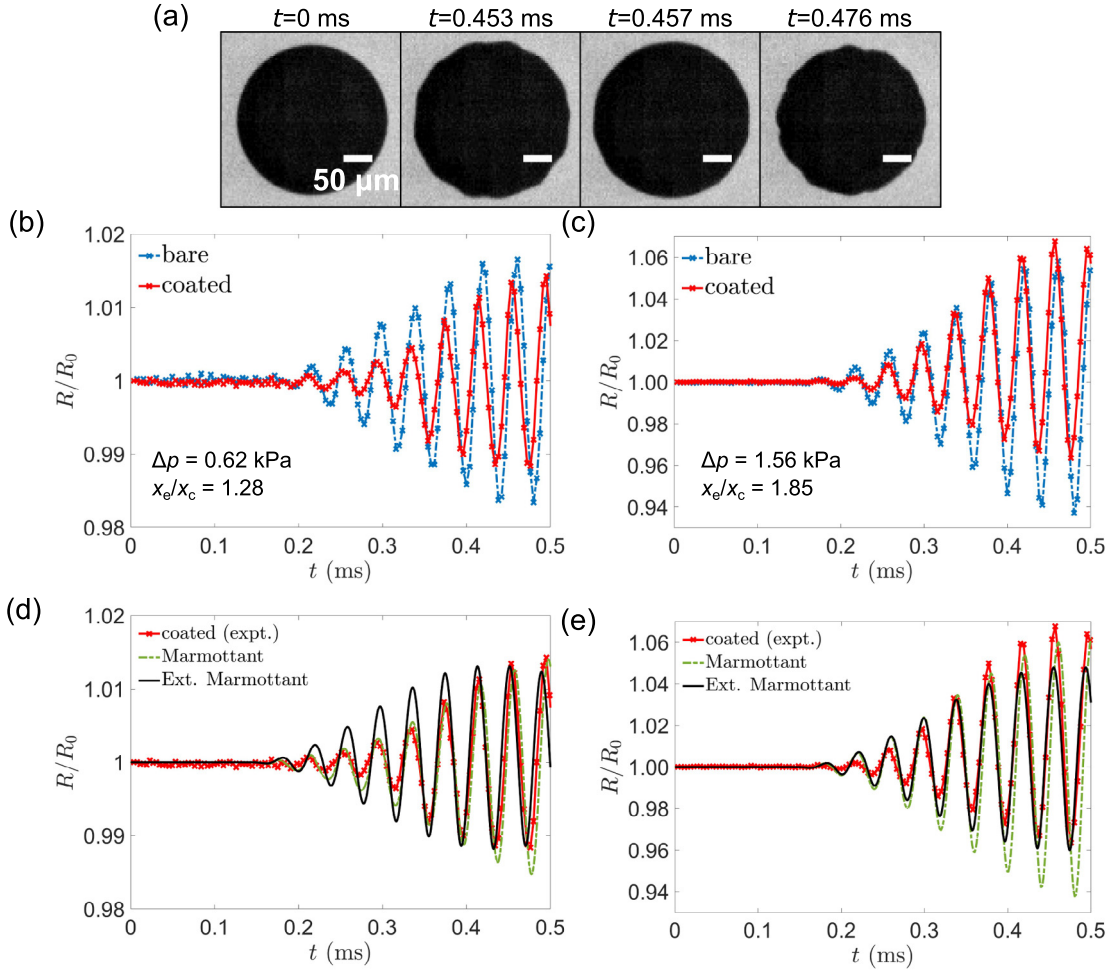

Fig. 4. Coated bubble oscillations. (a) Image sequence of oscillations for a colloid-coated bubble of radius $R_0 = 132\mu$m, coated by $2a = 5\mu$m colloids. Radius-time curves (red solid line) of the same bubble for (b) $\Delta p = 0.62 \pm 0.09$ kPa, resulting in $x_e/x_c = 1.28$; (c) $\Delta p = 1.56 \pm 0.22$ kPa, leading to $x_e/x_c = 1.85$. The radial dynamics for bare bubbles (blue dotted-dashed curve) of the same size are also shown. The Marmottant (green dashed curve) and the extended Marmottant model (black curve) models are compared to the coated bubble oscillations for the two pressures in (b,c) in (d,e) respectively. The values of the fitted parameters are provided in Section (4.2). The error bars on R/R_0 are smaller than the symbols.

non-linear behaviour for the small pressure amplitudes, $\Delta p = 0.62, 1.56$ kPa, at which bare bubbles show linear behaviour. Specifically, while bare bubbles exhibit symmetric oscillations around R_0 [Figure S2(c)], colloid-coated bubbles show *expansion-only* behaviour, where the extent of expansion is greater than the extent of compression. The term expansion-only (although there is also compression) is used in keeping with the literature on lipid-coated bubbles, where the term *compression-only* was coined

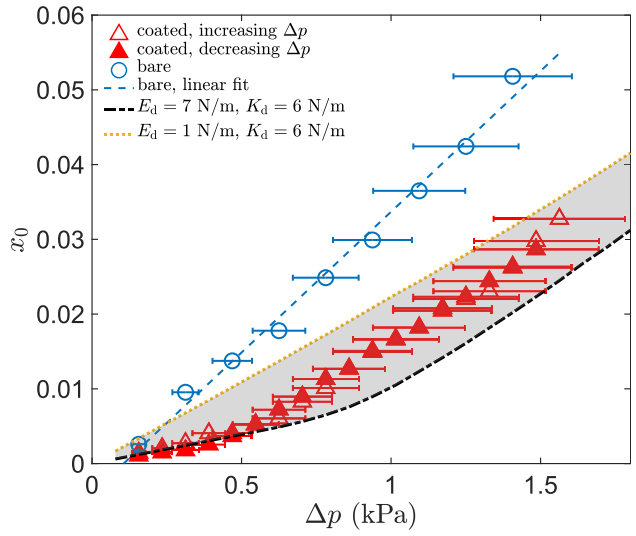

Fig. 5. Pressure sweep on colloid-coated bubbles. A coated bubble, with $R_0 = 134.7\mu$m and coated by $2a = 5\mu$m colloids, is subjected to increasing acoustic pressures (open red triangles) and then to decreasing pressures (filled red triangles). For comparison, experimental results for a bare bubble of the same radius (open blue circles) is shown for each case, with the linear fit to the data (blue dashed line). The error bars on x_0 are smaller than the symbols. Model predictions are shown for high estimate of $E_d = 7$N/m (black dotted-dashed line) and lower estimate of $E_d = 1$N/m (orange dotted line). In both cases $K_d = 6$N/m. The coated bubble data lie between these two theoretical bounds, as shown by the shaded region.

to refer to the opposite behaviour, when the extent of compression is larger than the extent of expansion [35] (although there is also expansion). This non-linear effect can be quantified as the ratio of the extent of expansion, $x_e = (R_{max} - R_0)/R_0$, to the extent of compression $x_c = (R_0 - R_{min})/R_0$. For the colloid-coated bubbles, $x_e/x_c > 1$ for all particle sizes considered (see Supplementary Material, Figures S4 and S5). In addition to expansion-only behaviour, another non-linear behaviour is observed in Fig. 4(b): for $\Delta p = 0.62$ kPa, the expansion amplitude is significantly reduced in comparison with the bare bubble. For the same bubble, this effect diminishes at $\Delta p = 1.56$ kPa, which indicates that the monolayer stiffness can decrease with increasing stress, compatible with strain-softening behaviour [50].

The constitutive models described in Section (2) are compared with the experimental coated bubble response in Figs. 4(d,e). Micrographs of the coated bubble interface (Supplementary Material, Figure S6) confirm that $R_{full} \approx R_0$, and therefore the equilibrium surface stress is taken to be $\sigma(R_0) = \sigma(R_{full}) = 10$mN/m, as measured from pendant drop experiments (described in Supplementary Material). The micrographs in Figure S6 also show small out-of-focus areas of the monolayer, where the particles are displaced out of the plane of the interface, indicating that the monolayer compression is slightly beyond full coverage. From the images it is clear that the particles are out of plane by less than a particle radius a, but the effect is difficult to quantify more precisely and the resulting pre-stress is not included in the model.

For $\Delta p = 0.62$ kPa with $x_e/x_c = 1.28$ in the experiment, the Marmottant model [Eq. (5)] shows good fit for $E_d \approx 15$N/m and

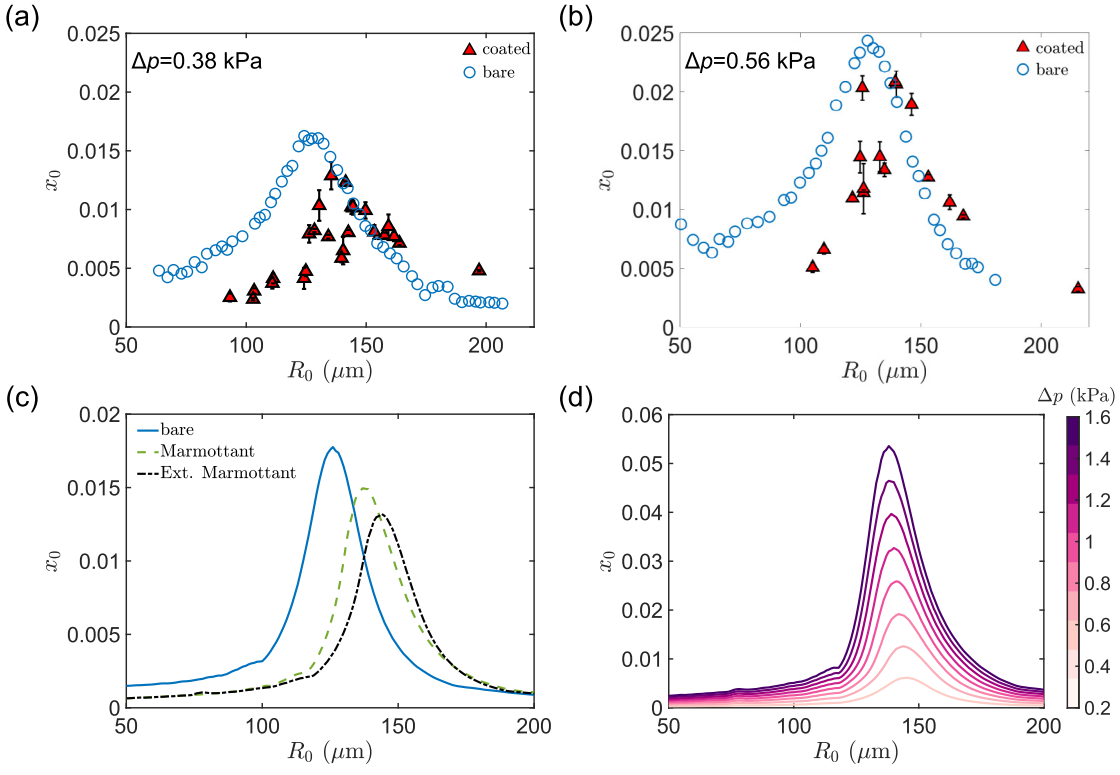

Fig. 6. Radius sweep. (a-b) Experimental resonance curves for coated bubbles (red triangles) with particle size $2a = 2.4\mu$m, and bare bubbles (blue circles) for (a) $\Delta p = 0.38 \pm 0.03$ kPa and (b) $\Delta p = 0.56 \pm 0.05$ kPa. The error bars on x_0 for the bare bubbles are smaller than the symbols. For coated bubbles, each data point represents a different bubble and is the average of 3 repeats, with the error bars showing the standard deviation. (c) Numerical solution of the Rayleigh-Plesset equation to generate the radius-sweep results for bare (blue line), and incorporating the interfacial stresses using the Marmottant (green dashed line) and extended (black dotted-dashed line) models, for $\Delta p = 0.56$ kPa. Both models are able to explain the increase in resonance radius due to interfacial viscoelasticity. (d) The extended model also explains the skewness of the resonance curve with increasing pressure.

$\eta_d \approx 10^{-8}$kg/s, yet predicts compression-only behaviour with $x_e/x_c \approx 0.9$. Our extended Marmottant model, Eq. (7), predicts $x_e/x_c \approx 1.1$ for $E_d \approx 2$N/m, $K_d \approx 6$N/m and the same η_d. Thus, the extended model better accounts for the expansion-only behaviour. The initial stiffness (E_d) to expansion changes with increasing amplitude of the subsequent acoustic cycles, which is not accounted for by either of the models that assume constant moduli. At $\Delta p = 1.56$ kPa, when the dilational stiffness seems to disappear with increased expansion-only behaviour observed, $x_e/x_c = 1.85$, the extended model is better able to explain the experimental trends with $E_d \approx 0.01$N/m and $K_d \approx 4$N/m, leading to $x_e/x_c \approx 1.2$. Whereas, the Marmottant model still predicts symmetric behaviour with $x_e/x_c \approx 1$ for $E_d \approx 2$N/m.

4.3. Pressure-sweep with colloid-coated bubbles

Fig. 5 shows the pressure-sweep protocol applied to a bubble with $R_0 = 134.7\mu$m, coated by $2a = 5\mu$m colloids. The bubble exhibits reduced amplitude of oscillations with respect to its bare bubble counterpart (see also Supplementary Material, Figures S8 and S9). This is true for all three particle sizes considered (Supplementary Material, Figure S10). The increase in excursion amplitude is non-linear with pressure and is in agreement with the decrease in dilational modulus as noted in Section (4.2). As Δp increases, the bubble exhibits slight compression-only behaviour ($x_e/x_c = 0.98$ at $\Delta p = 0.47 \pm 0.07$ kPa), then symmetric and finally expansion-only behaviour ($x_e/x_c = 1.44$ at $\Delta p = 1.56 \pm 0.22$ kPa). This is captured by taking a high $E_d = 7$N/m and then later a lower $E_d = 1$N/m, with constant $K_d = 6$N/m. The data is seen to fall between these two regimes (shaded region). This more clearly illustrates the strain-softening behaviour of the colloid monolayer [50,51]. It is noted that the extended Marmottant model predicts compression-only, symmetric and expansion-only behaviours when the ratio E_d/K_d is less than, equal to or greater than unity, respectively. While the Marmottant model can predict compression-only when $E_d > 0$, it overestimates the compression. In the extended Marmottant model, the compression is bound to a lower limit by the presence of K_d.

4.4. Radius-sweep with colloid-coated bubbles

Fig. 6(a) shows the radius-sweep protocol for bubbles coated by $2a = 2.4\mu$m colloids, contrasted with bare bubbles, for $\Delta p = 0.38 \pm 0.03$ kPa. For coated bubbles, each data point corresponds to an individual bubble. The resonance radius, R_0^{res}, is $\approx 8\%$ higher than that for bare bubbles, with the overall response being reduced for $R_0 < R_0^{res}$. The resonance curve becomes more skewed at higher pressure as seen in Fig. 6(b) for $\Delta p = 0.56 \pm 0.05$ kPa. These observations can be ascribed to the viscoelastic effects since both the Marmottant and the extended models are able to explain the increase in the resonance radius as seen in Fig. 6(c).

The skewness with increasing pressure also is captured with the extended model, in Fig. 6(d), and demonstrates that for colloid-coated bubbles, non-linear response can be expected even for strain amplitudes of 1–2%.

The radius-time curves for the 2.4μm colloid-coated bubbles were compared with the extended Marmottant model to get estimates for the viscoelastic parameters as $E_d \approx 5$N/m, $K_d \approx 4$N/m and $\eta_d \approx 10^{-8}$kg/s. The numerically generated curves were produced using a theoretical estimate for the polytropic exponent [49] while the viscosity was set to that of water. Thus, the theoretical curves do not capture the damping effects in the experiments, for both bare and coated bubbles. However, there is agreement with the trends in terms of increase in resonance radius when comparing the bare and coated cases. Since the current model does not incorporate strain-dependent viscoelastic parameters, the theoretical resonance curves were generated by fixing to the aforementioned values over all acoustic pressures. This is qualitatively able to capture the skewness of the curves.

4.5. Comparison with existing techniques

We now compare the high-frequency measurements by bubble dynamics with low-frequency measurements with existing techniques. For direct, quantitative comparison, we performed quasi-static measurements of the same colloidal system using drop-shape analysis. Because attractive interparticle interactions are dominant, and therefore the monolayer is elastic, we used the drop-shape fitting elastometry approach (DSFE) [10–12]. The details of these measurements are described in the Supplementary Material. In the literature, oscillatory interfacial rheological measurements on a water–air interface in a Langmuir trough are available for a similar system [41]. Before comparing numerical values of the interfacial elastic moduli, we need to establish if these experiments measure E_d or K_d.

In surface pressure-area isotherms of particle monolayers [41,42,46], three regimes are typically identified: first, a slow increase in slope as particles interact through long-range interactions (Regime I); next, as the particles are sufficiently close to experience strong repulsive interactions, the slope increases rapidly (Regime II); and finally, the slope abruptly decreases when the monolayer undergoes large-scale buckling (Regime III). The regime of *particle-scale* buckling would then lie between Regime II and Regime III but is not clearly identifiable in surface pressure-area isotherms, possibly because it occurs for a very small range of areas. On the other hand, for quasi-static compression of armoured drops and bubbles [27,29], the regime of particle-scale buckling can be observed, because of the controlled application of strains comparable to the particles sizes. Therefore, we expect that the interfacial dilatational elasticity that is measured with Langmuir trough and pendant drop methods is typically E_d.

Our measurements with DSFE on pendant drops give $E_d \approx 100$ mN/m (see Figure S7 in Supplementary Materials) for the same particle size ($2a = 5$ μm) and electrolite concentration (500 mM NaCl) as in our bubble-dynamics experiments. The Langmuir trough measurements of Ref. [41] are for 1 μm polystyrene particles with sulfate groups, and electrolyte concentration of 1 M NaCl. The elastic modulus in this experiment is $E_d \approx 350$mN/m, if we assume that the value of the real part of the complex modulus approaches the zero-frequency value at 0.1 Hz. Both these low-frequency values are smaller than the value of $E_d \approx 1 - 7$ N/m measured in the bubble-dynamics experiments. This suggests that the elasticity of the system considered here increases with increasing frequency.

5. Conclusions

We used an ultrasound-driven microbubble as an interfacial rheological probe to access non-linear phenomena of colloid monolayers at high frequency. This method is able to detect the change in rheological properties at high frequency of the colloid monolayer.

From the temporal evolution of the bubble radius it is clear that colloid-coated bubbles exhibit expansion-only behaviour, in contrast to the known compression-only behaviour observed for lipid-coated bubbles [37,35]. Compression of the colloid monolayer beyond maximum coverage causes buckling [44,27,29]. In a stress-sweep protocol, the expansion-only behaviour is seen to be most prominent at the upper end of the pressure interval, with

a non-linear increase in the excursion, consistent with strain-softening behaviour [50]. In a radius-sweep protocol, the resonance curve becomes more skewed with increasing pressure. Both protocols detect the non-linear response of the monolayer, which we described by a simple 1D model for the interfacial stress, incorporated into the Rayleigh-Plesset equation to describe the coated bubble dynamics.

The estimated value of the interfacial elasitc modulus at ultrasonic frequency ($f = 25$kHz) was found to be an order of magnitude larger than the value measured under quasi-static compression. While an increase in elastic moduli of soft matter systems at high-frequency has been previously reported for the bulk shear moduli of hydrogels [22,25] the micromechanical origin of this non-linear behaviour remains to be established for the colloid-monolayer system.

Future work should test the applicability of this method to soluble and insoluble monolayers of other surface active species. The portfolio of protocols illustrated here provides a means for interrogating the complex micromechanical behaviour of structured interfaces under highly unsteady conditions and complements other high-frequency dilational interfacial rheological techniques.

Declaration of Competing Interest

The authors declare that they have no known competing financial interests or personal relationships that could have appeared to influence the work reported in this paper.

Acknowledgments

The Authors thank Y.-F. Lee for helpful discussions. This work was funded by ERC StG No. 639221 (V.G.).

Appendix A. Supplementary material

Supplementary data associated with this article can be found, in the online version, at https://doi.org/10.1016/j.jcis.2022.10.093.

Appendix B. Data availability

The datasets generated and analyzed in this study are available at the 4TU.ResearchData repository at: https://doi.org/10.4121/21387384.

References

[1] L.M.C. Sagis, Dynamic properties of interfaces in soft matter: Experiments and theory, Rev. Mod. Phys. 83 (2011) 1367–1403.
[2] G.G. Fuller, J. Vermant, Complex Fluid-Fluid Interfaces: Rheology and Structure, Annu. Rev. Chem. Biomol. Eng. 3 (1) (2012) 519–543.
[3] Y.-J. Lin, S. Barman, P. He, Z. Zhang, G.F. Christopher, S.L. Biswal, Combined interfacial shear rheology and microstructure visualization of asphaltenes at air-water and oil-water interfaces, J. Rheol. 62 (1) (2018) 1–10.
[4] C.-C. Chang, A. Nowbahar, V. Mansard, I. Williams, J. Mecca, A.K. Schmitt, T.H. Kalantar, T.-C. Kuo, T.M. Squires, Interfacial rheology and heterogeneity of aging asphaltene layers at the water–oil interface, Langmuir 34 (19) (2018) 5409–5415.
[5] H. Wang, X. Wei, Y. Du, D. Wang, Experimental investigation on the dilatational interfacial rheology of dust-suppressing foam and its effect on foam performance, Process Saf. Environ. Prot. 123 (2019) 351–357.
[6] P. Bertsch, P. Fischer, Interfacial rheology of charged anisotropic cellulose nanocrystals at the air–water interface, Langmuir 35 (24) (2019) 7937–7943.
[7] D. Renggli, A. Alicke, R.H. Ewoldt, J. Vermant, Operating windows for oscillatory interfacial shear rheology, J. Rheol. 64 (1) (2020) 141–160.
[8] P. Cicuta, E.J. Stancik, G.G. Fuller, Shearing or compressing a soft glass in 2d: Time-concentration superposition, Phys. Rev. Lett. 90 (2003) 236101.
[9] S. Reynaert, P. Moldenaers, J. Vermant, Interfacial rheology of stable and weakly aggregated two-dimensional suspensions, Phys. Chem. Chem. Phys. 9 (2007) 6463–6475.
[10] S. Knoche, D. Vella, E. Aumaitre, P. Degen, H. Rehage, P. Cicuta, J. Kierfeld, Elastometry of deflated capsules: Elastic moduli from shape and wrinkle analysis, Langmuir 29 (40) (2013) 12463–12471.
[11] M. Nagel, T.A. Tervoort, J. Vermant, From drop-shape analysis to stress-fitting elastometry, Adv. Colloid Interface Sci. 247 (May) (2017) 33–51.
[12] J. Hegemann, S. Knoche, S. Egger, M. Kott, S. Demand, A. Unverfehrt, H. Rehage, J. Kierfeld, Pendant capsule elastometry, J. Colloid Interface Sci. 513 (2018) 549–565.
[13] T. Verwijlen, L. Imperiali, J. Vermant, Separating viscoelastic and compressibility contributions in pressure-area isotherm measurements, Advances in Colloid & Interface Science 206 (2014) 428–436.
[14] N. Jaensson, J. Vermant, Tensiometry and rheology of complex interfaces, Curr. Opin. Colloid Interface Sci. 37 (2018) 136–150.
[15] V. Garbin, Collapse mechanisms and extreme deformation of particle-laden interfaces, Current Opinion in Colloid & Interface Science 39 (2019) 202–211.
[16] I. Buttinoni, Z.A. Zell, T.M. Squires, L. Isa, Colloidal binary mixtures at fluid–fluid interfaces under steady shear: structural, dynamical and mechanical response, Soft Matter 11 (2015) 8313–8321.
[17] S. Saha, F. Pagaud, B.P. Binks, V. Garbin, Buckling versus crystal expulsion controlled by deformation rate of particle-coated air bubbles in oil, Langmuir 38 (3) (2022) 1259–1265.
[18] D. Langevin (Ed.), Light Scattering by Liquid Surfaces and Complementary Techniques, Marcel Dekker, 1992.
[19] N. Abi Chebel, A. Piedfert, B. Lalanne, C. Dalmazzone, C. Noïk, O. Masbernat, F. Risso, Interfacial dynamics and rheology of a crude-oil droplet oscillating in water at a high frequency, Langmuir 35 (29) (2019) 9441–9455.
[20] J.S. Lum, J.D. Dove, T.W. Murray, M.A. Borden, Single microbubble measurements of lipid monolayer viscoelastic properties for small-amplitude oscillations, Langmuir 32 (37) (2016) 9410–9417.
[21] B. Dollet, P. Marmottant, V. Garbin, Bubble dynamics in soft and biological matter, Annu. Rev. Fluid Mech. 51 (1) (2019) 331–355.
[22] A. Jamburidze, M. De Corato, A. Huerre, A. Pommella, V. Garbin, High-frequency linear rheology of hydrogels probed by ultrasound-driven microbubble dynamics, Soft Matter 13 (2017) 3946–3953.
[23] B. Saint-Michel, V. Garbin, Acoustic bubble dynamics in a yield-stress fluid, Soft Matter 16 (2020) 10405–10418.
[24] B. Saint-Michel, V. Garbin, Bubble dynamics for broadband microrheology of complex fluids, Current Opinion in Colloid & Interface Science 50 (2020) 101392.
[25] L. Mancia, J. Yang, J.-S. Spratt, J.R. Sukovich, Z. Xu, T. Colonius, C. Franck, E. Johnsen, Acoustic cavitation rheometry, Soft Matter 17 (2021) 2931–2941.
[26] S.M. van der Meer, B. Dollet, M.M. Voormolen, C.T. Chin, A. Bouakaz, N. de Jong, M. Versluis, D. Lohse, Microbubble spectroscopy of ultrasound contrast agents, The Journal of the Acoustical Society of America 121 (1) (2007) 648–656.
[27] O. Pitois, M. Buisson, X. Chateau, On the collapse pressure of armored bubbles and drops, The European Physical Journal E 38 (5) (2015) 1–7.
[28] V. Poulichet, V. Garbin, Ultrafast desorption of colloidal particles from fluid interfaces, Proceedings of the National Academy of Sciences of the United States of America 112 (19) (2015) 5932–5937.
[29] N. Taccoen, F. Lequeux, D.Z. Gunes, C.N. Baroud, Probing the mechanical strength of an armored bubble and its implication to particle-stabilized foams, Physical Review X 6 (1) (2016) 1–11.
[30] P.J. Beltramo, M. Gupta, A. Alicke, I. Liascukiene, D.Z. Gunes, C.N. Baroud, J. Vermant, Arresting dissolution by interfacial rheology design, Proceedings of the National Academy of Sciene 114 (39) (2017) 10373–10378.
[31] A. Huerre, M. De Corato, V. Garbin, Dynamic capillary assembly of colloids at interfaces with 10,000g accelerations, Nature Communications 9 (1)(2018) 1–9.
[32] M.S. Plesset, A. Prosperetti, Bubble dynamics and cavitation, Annu. Rev. Fluid Mech. 9 (1) (1977) 145–185.
[33] A. Prosperetti, Thermal effects and damping mechanisms in the forced radial oscillations of gas bubbles in liquids, J. Acoust. Soc. Am. 61 (1) (1977) 17–27.
[34] M. Versluis, E. Stride, G. Lajoinie, B. Dollet, T. Segers, Ultrasound contrast agent modeling: A review, Ultrasound in Medicine & Biology 46 (9) (2020) 2117–2144.
[35] P. Marmottant, S. van der Meer, M. Emmer, M. Versluis, N. de Jong, S. Hilgenfeldt, D. Lohse, A model for large amplitude oscillations of coated bubbles accounting for buckling and rupture, The Journal of the Acoustical Society of America 118 (6) (2005) 3499–3505.
[36] K.Y.C. Lee, Collapse mechanisms of Langmuir monolayers, Annu. Rev. Phys. Chem. 59 (1) (2008) 771–791.
[37] N. de Jong, M. Emmer, C.T. Chin, A. Bouakaz, F. Mastik, D. Lohse, M. Versluis, Compression-Only Behavior of Phospholipid-Coated Contrast Bubbles, Ultrasound Med. Biol. 33 (4) (2007) 653–656.
[38] M. Overvelde, V. Garbin, J. Sijl, B. Dollet, N. de Jong, D. Lohse, M. Versluis, Nonlinear shell behavior of phospholipid-coated microbubbles, Ultrasound in Medicine & Biology 36 (12) (2010) 2080–2092.
[39] Y. Luan, T. Faez, E. Gelderblom, I. Skachkov, B. Geers, I. Lentacker, T. van der Steen, M. Versluis, N. de Jong, Acoustical Properties of Individual Liposome-Loaded Microbubbles, Ultrasound Med. Biol. 38 (12) (2012) 2174–2185.
[40] P. Pieranski, Two-dimensional interfacial colloidal crystals, Phys. Rev. Lett. 45 (7) (1980) 569–572.
[41] A.G. Bykov, B.A. Noskov, G. Loglio, V.V. Lyadinskaya, R. Miller, Dilational surface elasticity of spread monolayers of polystyrene microparticles, Soft Matter 10 (2014) 6499–6505.
[42] C. Monteux, J. Kirkwood, H. Xu, E. Jung, G.G. Fuller, Determining the mechanical response of particle-laden fluid interfaces using surface pressure

isotherms and bulk pressure measurements of droplets, Phys. Chem. Chem. Phys. 9 (2007) 6344–6350.
[43] A.C. Martinez, E. Rio, G. Delon, A. Saint-Jalmes, D. Langevin, B.P. Binks, On the origin of the remarkable stability of aqueous foams stabilised by nanoparticles: Link with microscopic surface properties, Soft Matter 4 (7) (2008) 1531–1535.
[44] S.T. Milner, J.F. Joanny, P. Pincus, Buckling of Langmuir monolayers, Europhysics Letters (EPL) 9 (5) (1989) 495–500.
[45] M. Abkarian, A.B. Subramaniam, S.-H. Kim, R.J. Larsen, S.-M. Yang, H.A. Stone, Dissolution arrest and stability of particle-covered bubbles, Phys. Rev. Lett. 99 (2007) 188301.
[46] R. Mears, I. Muntz, J.H.J. Thijssen, Surface pressure of liquid interfaces laden with micron-sized particles, Soft Matter 16 (2020) 9347–9356.
[47] B.L. Helfield, B.Y. Leung, D.E. Goertz, The effect of boundary proximity on the response of individual ultrasound contrast agent microbubbles, Physics in Medicine and Biology 59 (7) (2014) 1721–1745.
[48] D. Baresch, V. Garbin, Acoustic trapping of microbubbles in complex environments and controlled payload release, Proceedings of the National Academy of Sciences 117 (27) (2020) 15490–15496.
[49] F. Hamaguchi, K. Ando, Linear oscillation of gas bubbles in a viscoelastic material under ultrasound irradiation, Physics of Fluids 27 (11) (2015) 113103.
[50] L.M. Sagis, P. Fischer, Nonlinear rheology of complex fluid-fluid interfaces, Curr. Opin. Colloid Interface Sci. 19 (6) (2014) 520–529.
[51] L.M. Sagis, E. Scholten, Complex interfaces in food: Structure and mechanical properties, Trends Food Sci. Technol. 37 (1) (2014) 59–71.